Materials and Design 197 (2021) 109188

Contents lists available at ScienceDirect

Materials and Design

journal homepage: www.elsevier.com/locate/matdes

Multi-method characterization approach to facilitate a strategy to design mechanical and electrical properties of sintered copper

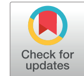

A. Wijaya [a], B. Eichinger [b], F.F. Chamasemani [a], B. Sartory [a], R. Hammer [a], V. Maier-Kiener [c], D. Kiener [c], M. Mischitz [b], R. Brunner [a,*]

[a] *Materials Center Leoben, Forschung GmbH, Leoben, Austria*
[b] *Infineon Technologies Austria AG, Austria*
[c] *Department of Materials Science, Montanuniversität Leoben, Leoben, Austria*

HIGHLIGHTS

- We present a multi-method characterization approach to understand the morphology-property relationship of sintered copper.
- We facilitate a strategy to design relevant material parameters for sintered copper films by tuning the morphology.
- We obtain a quantified insight about the effect of the heterogeneous morphologies on the investigated material properties.

GRAPHICAL ABSTRACT

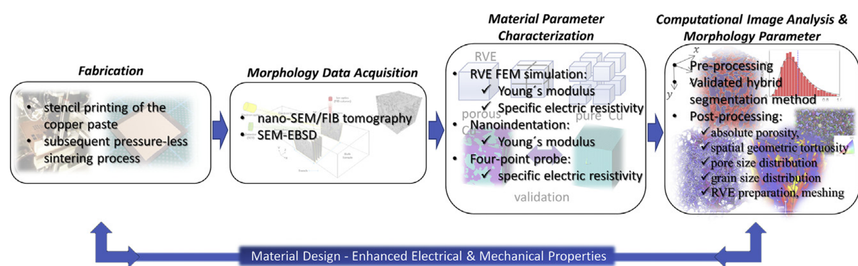

ARTICLE INFO

Article history:
Received 19 May 2020
Received in revised form 30 August 2020
Accepted 23 September 2020
Available online 28 September 2020

Keywords:
Sintered materials
Computational image analysis
Tomography
Elastic modulus
Specific electrical resistivity
RVE finite element method

ABSTRACT

Advanced die application materials, utilizing pressure-less sintered copper, show great prospects regarding cost effectiveness, power density, withstanding high switching speeds and temperature loading for novel eco-friendly and high efficiency semiconductors. In general, to preserve high reliability in combination with electrical functionality the design of elastic as well as electrical material parameters is of great importance. Here, we present a multi-method characterization approach to understand the impact of the morphology on the elastic as well as electrical behavior, which facilitates a strategy to design the relevant material parameters by tuning the morphology. Nano-SEM/FIB tomography and SEM/EBSD are applied to probe the morphology of three representative copper films. Nanoindentation and 4-point probe are used to extract the elastic modulus and specific electrical resistivity, respectively. The evaluated material parameters are compared with modeling results using the analyzed image data as an input. For the crucial image analysis, we develop a validated objective image analysis workflow. We obtain a quantified insight about the effect of the heterogeneous morphologies on the elastic modulus and specific electrical resistivity, thereby delivering important information about the necessary homogeneous copper morphology- and nano-scale pore-design. The strategy shall provide design guidelines to ensure reliable and high-performance die attachments.

© 2020 The Author(s). Published by Elsevier Ltd. This is an open access article under the CC BY license (http://creativecommons.org/licenses/by/4.0/).

* Corresponding author.
E-mail address: roland.brunner@mcl.at (R. Brunner).

https://doi.org/10.1016/j.matdes.2020.109188
0264-1275/© 2020 The Author(s). Published by Elsevier Ltd. This is an open access article under the CC BY license (http://creativecommons.org/licenses/by/4.0/).

1. Introduction

Porous materials have attracted great attention for various applications, e.g., catalysis [1], novel materials [2,3], energy related topics [4,5], acoustics [6], microelectronics [7,8], actuators [9], bioengineering [10], and biomimetic [11]. Recently, porous materials have gained interest as interconnect materials for power semiconductor devices [12]. The trend in the semiconductor industry goes towards eco-friendliness and higher energy efficiency [13]. Semiconductor compound materials, such as silicon carbide (SiC) or gallium nitride (GaN), pave novel possibilities in this manner with operation temperatures above 200 °C [14,15]. However, such high temperatures trigger challenges with respect to the use of conventional solders, e.g. decreased solder joint reliability and low conductivity result. In order to keep the trend going, novel material concepts are necessary. The use of sinter pastes display a promising alternative to conventional soldering techniques [16]. Sintered materials show potential to withstand high switching speeds, temperature loading and power density [17]. Silver (Ag) sinter pastes display possible candidates [18], but they are expensive to manufacture because they need high pressure during sintering to ensure sufficient bonding [18]. A possibility to solve this problem is the use of pressure-less sintered copper (Cu). Recent results show for low temperature pressure-less sintered Cu, that a specific electric resistivity of 4.3 μΩ.cm becomes feasible [7].

The formation of residual stress [19] leads to adhesion problems and cracks [19,20], and further results in insufficient thermal management [21]. The compliance of the material is important for the reliability to arrest *e.g.* crack formation or other failure modes. The challenge is to design a sintered copper film which provides a low elastic modulus [22], as well as low specific electrical resistivity [23]. In general, an understanding of the morphology-property relationship is critical to facilitate improved material design and increased reliability. Image-based characterization methods are highly capable to provide information about the morphology of porous materials [24–27]. However, the porous structure of the sintered material on μm to nm-scale makes the characterization of the morphology and its automatized quantification challenging, e.g. the correct computational treatment of so-called shine through artefacts which appear in scanning electron microscopy (SEM) and nano-scanning electron microscopy/focused ion beam (SEM/FIB)-tomography image data. Therefore, the development and application of a multi-method approach including advanced high-resolution imaging methods for the morphology analysis, experimental material parameter characterization and modeling is crucial for a persuasive design strategy. This also implies for the quantification of the obtained image data the development of an accurate and objective image analysis workflow.

In this paper we present a multi-method characterization approach to understand the impact of the morphology on the elastic as well as electrical behavior which facilitates a strategy to design the relevant material parameters by tuning the morphology. Nano-SEM/FIB tomography and SEM combined with electron backscatter diffraction (EBSD) are applied to probe the morphology of three representative copper films. Nanoindentation and 4-point probe are used to extract the elastic modulus and specific electrical resistivity, respectively. We compare the experimentally evaluated material parameters with modeling results using the analyzed image data as an input. For the crucial image analysis, we develop a validated objective image analysis workflow based on a hybrid image analysis algorithm. We obtain a quantified insight about the effect of the heterogeneous morphologies on the elastic modulus and specific electrical resistivity, thereby delivering important information about the necessary homogeneous copper grain- and nano-scale pore-design.

2. Characterization methods

The porous copper films are manufactured on a [100] silicon (Si) substrate, with 8-in. format (diameter of 200 mm), by stencil printing of the copper paste and a subsequent pressure-less sintering process [28]. All samples are cured at an elevated temperature of 400 °C in nitrogen atmosphere. The used paste, additives like solvents, and organic components, mainly define the samples' morphologies. We present three different sintered copper films labeled as A, B, and C. The thicknesses of the copper films A, B, and C are measured with a DektakXT Stylus Surface Profilometer on the manufactured 8-in. wafer. The layer thickness is measured by scanning the step height between the substrate level and the printed copper surface. The resulting mean thicknesses of sample A, B, and C depends on the used paste material and provides 21.0 ± 1.7 μm, 30.8 ± 1.7 μm and 12.4 ± 0.9 μm , respectively.

2.1. Nano-SEM/FIB tomography and SEM/EBSD

We use a cross-beam scanning electron microscope (SEM) from Zeiss (AURIGA® - CrossBeam workstation) for the nano-SEM/FIB tomography and electron backscatter diffraction (EBSD) experiments. For tomography experiments, we extract pieces (few mm^2) from the 8-in. wafer. Subsequently we pre-shape each sample into a cubic shape of $20 \times 20 \times 20$ μm^3 using Ga^+ ion milling with a current and voltage of 2 nA and 30 kV, respectively. The angle between the FIB and SEM columns is 54°. A platinum layer is deposited on top of the sample to reduce charging. In order to reduce noise, we apply a line average technique with scan speed 8 and $N = 1$. We can achieve a duration of about 8 h per sample, which includes the pre-shaping of the sample and the image data acquisition for the 3D reconstruction. No significant drift is observed. The SEM imaging is operated with a Secondary Electrons Secondary Ions (SESI) detector and an acceleration voltage of 30 kV. The voxel sizes in x- and y- direction are 9.3 nm and 11.5 nm (after 54° detector angle correction), respectively. The smallest incremental cutting distance is 50 nm in z- direction. We mill the cube slice by slice to obtain the 2D image slice stack.

EBSD is used to provide important data about the grain size, and grain orientation [29]. For the EBSD measurements, we use the cross-beam SEM (AURIGA® - CrossBeam workstation) from Zeiss equipped with a Hikari Super EBSD detector from EDAX. After the cross sectional cut with the ion beam, the sample surface is tilted at 70° to the detector. The accelerating voltage is set to 20 kV. The incident beam current is 20 nA. The frame averaging is 2 with step sizes of 100 nm. The Hough resolution is set to 96 and the camera resolution is 1024×1024 pixels with a pixel size of 50 nm. We extract the grain diameters by using 15° as the threshold for grain separation.

2.2. Nanoindentation and 4-point probe electrical measurements

The nanoindentation experiments to determine the elastic modulus are performed using the KEYSIGHT NanoIndenter G200 equipped with a continuous stiffness measurement (CSM) unit. The indentation is done using a standard three-sided Berkovic diamond tip (Synton-MDP) at room temperature. For the data analysis, the NanoSuite software is used. The area function of the tip is obtained by pre-indentation on a fused quartz using the standard value of the elastic modulus (72 GPa) [30]. In order to stabilize the nanoindentation experiments and gain a covariance of less than 10 %, we infiltrate the samples with an epoxy resin in vacuum. The maximum indentation strain rate was 0.05 /s and the CSM frequency is set to 45 Hz with an amplitude of 2 nm. A range between 800 and 1000 nm is chosen for the indentation depth. Ten indentation measurements are performed per sample for statistical reasons. The contact area for the Berkovic diamond tip shows a diameter of about 7 μm (1000 nm indentation depth).

The electrical measurements are performed using a 4-point probe resistivity setup and each sample is measured 8 times at random locations on the fabricated 8-in. wafer. The tungsten tips are set with 10 mm equidistance from each other and a source meter (Keithley 2400) probes

the sheet resistivity R_s. We use the formula $\rho_{porous} = \frac{\pi \cdot t}{\ln 2} R_s$ [31] with the thickness t, to measure the specific resistivity ρ_{porous} of the porous films.

2.3. Image analysis workflow

We put effort on the development of a validated image analysis workflow (Fig. 1) incorporating a hybrid segmentation technique which provides objective and accurate results with respect to the morphology analysis. The image processing is performed in three steps: (1) pre-processing, (2) thresholding and segmentation, and finally (3) 3D reconstruction and validation. The reconstruction of the 3D data is part of the image pre-processing step (Fig. 1(a)). It includes, image-stacking, −alignment, and −cropping using Avizo 2019.1. We reduce the shadowing artefacts by aligning the histogram peaks of all image slices in the x-, y- and z- plane to get uniform grey values in the image data using Python. Subsequently we apply non-local means filter to reduce the curtaining artefact to enhance the image quality. For statistical reasons, we analyze the largest possible volume of interest (VOI) at different locations on the wafer. The VOIs vary due to the different thickness of the fabricated films. The minimum and maximum size of the VOI are about 2500 and 13,500 μm^3, respectively. In Fig. 2 (a) we show representative pre-processed slice images for sample A, B and C. Critical is the segmentation of the nano-SEM/FIB tomography data. We use the pre-processed data (Fig. 1(a)) and generate the second derivative of the histogram (Fig. 1 (b)). The threshold between pores and the copper is extracted according the grey value of the first peak in the generated second derivative graph. Next, we apply the quickshift (QS) [32] algorithm in particular to eliminate the shine through artefacts. Those artefacts make the segmentation process and selection of the correct threshold difficult, since fore- and background information are hardly automatically resoluble. Other examples of super-pixel segmentation methods are Felzenszwalb & Huttenlocher (FH) [33], and simple linear iterative clustering (SLIC) [34]. QS represents a superpixel method by grouping similar pixels in color- and spatial distance [32]. The QS provides a perceptually tessellation of image data, thereby reducing the number of image primitives for subsequent image processing. With the QS, the pores and shine-through artefacts are segmented together in one segment. We calculate the pixels mean value of those segments. Finally, we segment the areas as pore if their average grey values are lower than the second derivative method thresholds.

For validation of the segmentation results, we perform manual segmentation as a ground truth (GT) and calculate the precision and recall (Fig. 1(c)). Precision is the ratio of true positive (TP) over the results of the segmentation method (RM). Recall is the ratio of TP over GT. The image analysis workflow provides a precision for sample A, B, and C of 94 %, 93 %, and 93 %, respectively and a recall of 88 %, 88 % and 97 %, respectively. The application of Otsu, Entropy, or IsoData [35–37], exhibits a recall only between 60% and 70% for sample A, B and C.

Fig. 2(b) shows exemplary for sample C the reconstructed 3D volume of interest (VOI) and the projection of the segmented pore area (red) on top of the SEM images in three different planes (z-y-, x-z-, and x-y-plane) to highlight the accuracy of our image analysis algorithm. The illustrated dimension of the VOI is used throughout the paper.

The skeletonization [38] and watershed algorithm [39] are applied to obtain the pore morphology parameters like the mean pore diameter and pore size distribution. A suitable measure with respect to the conductivity of the copper strut is the geometric tortuosity [40]. The geometric tortuosity between two points is defined by the ratio of the

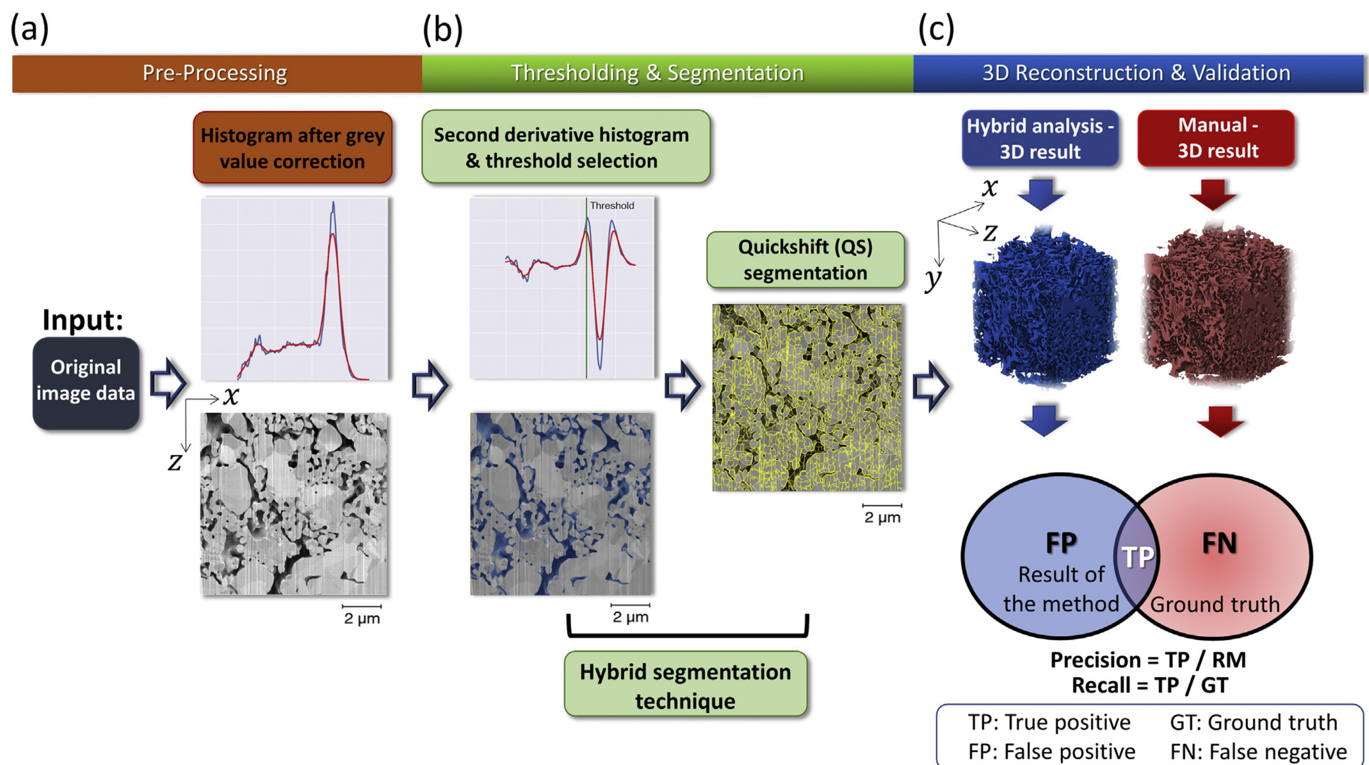

Fig. 1. Image analysis workflow which consists of (a) pre-processing, (b) thresholding and segmentation as well as (c) 3D reconstruction and validation. (a) Pre-processing includes image-stacking, −alignment, and −cropping. Shadowing artefacts are reduced by aligning the histogram peaks of all image slices in three (x-, y- and z-) planes in order to get uniform grey values. Non-local means filters are applied to reduce the curtaining artefact to enhance the image quality. (b) Thresholding and segmentation: Second derivative of the histogram is used. The threshold between pores and the copper is extracted according the grey value of the first peak in the generated second derivative graph. Quickshift (QS) segmentation is performed to increase the recall. Since the segmentation combines two approaches (second derivative and QS) it is defined as a hybrid segmentation technique. The two segmentation methods are combined to get the final result. (c) 3D reconstruction and validation: 3D reconstruction from the obtained 2D slice stack data. For validation the precision and recall are calculated to measure the relevance of the image analysis workflow. Manually segmented 3D data is used as a ground truth.

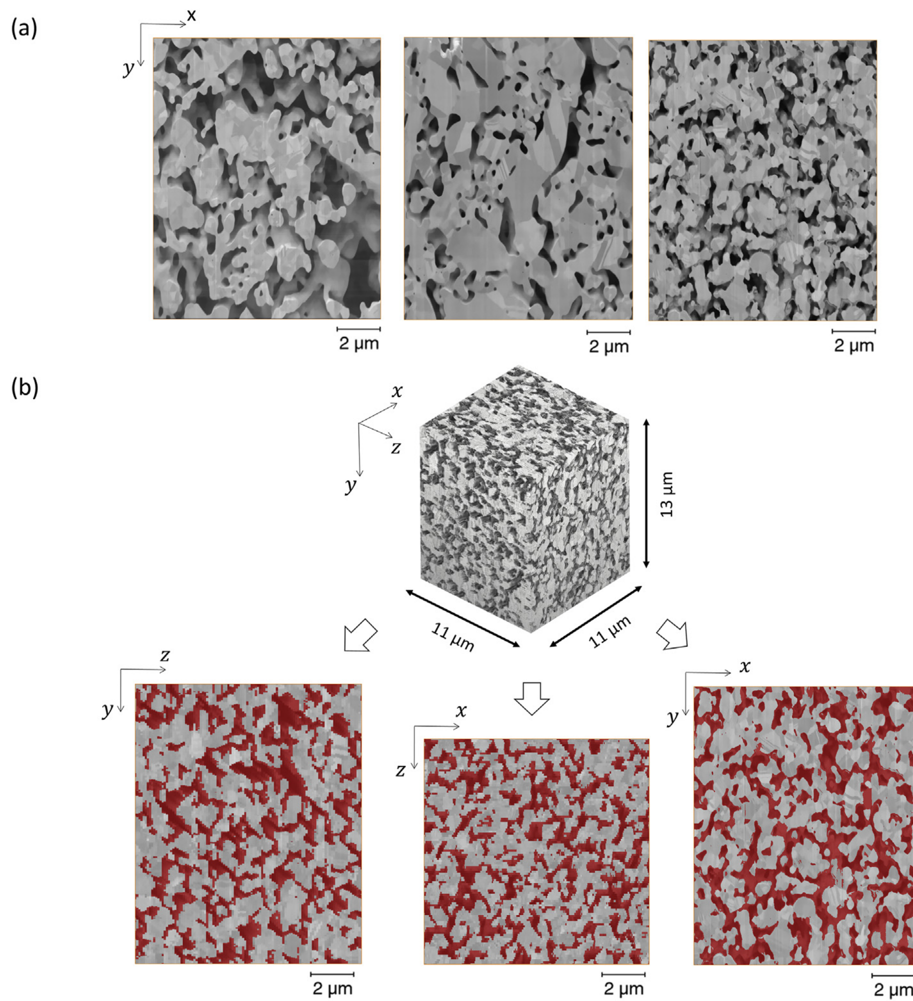

Fig. 2. Pre-processed SEM/FIB tomography image data (a) in the *x*-*y*-plane for sample A (left), sample B (middle) and sample C (right). (b) 3D reconstructed VOI exemplarily for sample C. The dimensions of the VOI with about $11 \times 11 \times 13\,\mu m^3$ are shown. Below: Representative slice images for the *z*-*y*-, *x*-*z*- and *x*-*y*- plane. The segmented pore space (red) is projected on top of the reconstructed grey value image. (For interpretation of the references to color in this figure legend, the reader is referred to the web version of this article.)

geodesic distance (LG) and the Euclidean distance (LE). LG is the shortest path possible whereas LE gives the shortest linear distance without any interfering structure. The LG and LE for the copper are calculated for every segmented voxel within the VOI. The ratio of those values yields the tortuosity profiles in *x*-, *y*-, and *z*- direction [25]. For the evaluation of the tortuosity from the segmented 3D data, we use the scikit-fmm package from Python.

The EBSD data of porous materials contains false registered pore areas. We eliminate those artefacts by masking the pore area using Avizo 2019.1. The QS technique [32] is used to segment the grain boundaries. The separated grain area is measured and converted into an equivalent circular diameter [41].

2.4. Modeling of material parameters: RVE-FEM

For the modeling we use the finite element method (FEM) to simulate the elastic stiffness matrix and the specific electrical resistivity tensor based on the image analyzed 3D morphology data. FEM is able to reveal the response of the material by a set of test loadings on representative volume elements (RVEs). The RVE-FEM technique displays a favorite tool to assess material properties of complex porous structures [42]. In this study, the elastic constants and conductivities are revealed based on the segmented 3D morphology and the constitutive properties of the bulk copper (elastic modulus $E = 117$ GPa, Poisson ratio $\nu = 0.33$, specific resistivity $\rho = 1.72\ \mu\Omega.\text{cm}$) [43].

The segmented VOI is divided into 8 sub-volumes, allowing a statistical estimation of the error bounds for the computed elastic constants and specific electrical resistivity. The local material information for copper and the pores are assigned to sub-volume FE meshes with $50 \times 50 \times 50$ element cubes. Hexahedral, quadratic 20-node elements (Ansys solid 186 for the morphology and solid 231 for the electrical) are used. A customized Ansys APDL script is applied to assign the material data (copper and pore) locally to each element. In order to get elements with nearly quadratic aspect ratio, the size for all computations in *x*-, *y*-, and *z*- is 93 nm, 115 nm, and 100 nm, respectively.

To probe the mechanical response, the commonly known kinematic uniform boundary conditions (KUBC) with six independent loadings (3 uniaxial and 3 shear loadings) of small strain of 10^{-5} are applied. By reading out the resulting averaged stresses in all directions for a given strain, the stiffness matrix is constructed. The inverse gives the compliance matrix and the engineering elastic constants are computed according to known relationships [44]. To probe the electrical response, three independent loading conditions in the three orthogonal coordinate directions are applied on the RVE. Supplementary 2 shows the RVE-FEM simulation methods. Neither for the simulation of the elastic modulus nor for the electrical resistivity the grain morphology of the copper is considered.

3. Results

3.1. Experimental material parameter characterization

We extract the reduced elastic modulus E_{porous} of the resin infiltrated porous samples from the indentation curve. This approximation is sufficient, since the elastic modulus of the epoxy resin (E_{epoxy} = 3.5 GPa), is much smaller than the one from bulk copper (E_{Cu} = 116 GPa). In fact, simplifying the structure and assuming a parallel compound modulus, we would arrive at a resin contribution of less than 3 %, which is in the range of the data noise and seems thus negligible. There could be much larger artificial errors introduced from the assumed composite law in comparison to the actual structure. As such, it seems justified to not take the resin contribution into account. The results are summarized in Table 1. Sample A shows the lowest reduced elastic modulus with 14.8 ± 0.6 GPa. We obtain a reduced elastic modulus of 29.8 ± 0.5 GPa for sample C. Sample B shows the largest elastic modulus with about 33.8 ± 2.2 GPa.

The results of the specific electrical resistivity ρ_{porous} obtained from the 4-point probe measurements are also presented in Table 1. Sample A shows the highest specific electrical resistivity with 14.4 ± 1.9 μΩ.cm. Therefore, sample A would be less interesting for micro- or power electronics applications. For sample B, we observe a specific resistivity of about 6.0 ± 0.9 μΩ.cm. The lowest specific resistivity provides sample C with about 4.4 ± 1.5 μΩ.cm.

3.2. Quantitative 3D pore-morphology characterization: Nano-SEM/FIB tomography

Fig. 3(a) shows the 3D rendered binary data set with the segmented copper (dark blue) and pore phase (red) for the three samples. From the segmented 3D data sets, we evaluate the absolute porosity for each sample, which is defined by the ratio of the total pore volume to that of the bulk volume or volume of interest (VOI). In Table 1 we show the evaluated mean value of the absolute porosity and corresponding standard deviation. Sample A gives the most porous material with 55.0 ± 4.1 %. Sample B provides the smallest porosity with 31.2 ± 4.8 % and sample C gives a slightly higher porosity with 36.1 ± 1.7 %.

We analyze the 3D pore network morphology by using the watershed (Fig. 3(b)) and skeletonization (Fig. 3(c)) algorithm to determine the pore diameter distribution (Fig. 3(d)). The skeletonized 3D pore morphology (see Fig. 3(c)) of sample C suggests the most homogenous pore network in comparison to sample A and B.

With the watershed algorithm, the main pore network is segmented into its constituent pore space segments [45]. The pore space segments obtained from the watershed provide the possibility to quantify the morphology parameters e.g. the pore volume and pore diameter for each segment. We use the so-called hydraulic radius [47] which reflects a common measure of the pore size, to get an estimate of the quasi non-circular extension of the pore. The hydraulic radius is defined as the ratio of pore volume by the surface area of each pore segment, as expressed by the equation $r_{h,i} = \frac{V_{p,i}}{A_{p,i}}$, where $r_{h,i}$ is the average hydraulic radius, $V_{p,i}$ is the volume, and $A_{p,i}$ is the surface area for each segmented pore space segment i, with i = 1,2,3, … [47]. For a non-circular pore, the hydraulic diameter $d_{h,i}$ is customarily defined by $4.r_{h,i}$ [48]. In Table 2, the evaluated morphology parameters $\overline{r}_{p,watsh}$ and $\overline{d}_{p,watsh}$ are depicted, reflecting the mean of the hydraulic radius and diameter over all segmented pore segments. However, to obtain the individual pore segments correctly an appropriate bin parameter number needs to be selected [45]. Any over- or under-segmentation should be avoided (Supplementary 3). We validate the selected bin number of 2 by comparing the results from the skeletonization and watershed segmentation. In general, as shown in Table 2, the skeleton diameter provides smaller values than the one obtained from the watershed algorithm [46]. The mean diameter $\overline{d}_{p,skel}$ is defined by the mean of the counted smallest distances computed from the center line to the segmented copper interface and multiplied with the factor two. The diameter distribution in Fig. 3(d) is plotted and fitted with a log-normal distribution.

3.3. Quantitative grain morphology characterization: SEM/EBSD

In Fig. 4 we depict the grain morphology of the copper from the SEM/EBSD measurements and extract the corresponding grain size distribution using the presented image analysis approach. The inverse pole figure and image quality map (IPF-IQ) for all samples reveal an almost randomly orientated polycrystalline microstructure with no preferable orientation. The crystals orientation in [111], [001], and [101] are almost evenly distributed.

The grain size distribution follows a log-normal distribution. Sample A and C have similar standard deviations and slightly different mean grain size diameters with 244 ± 136 nm and 279 ± 146 nm, respectively. Both samples show a smaller grain size and standard deviation in comparison to sample B (382 ± 249 nm). This indicates that sample B exhibits a less homogeneous grain size distribution than sample A and C. The mean grain diameter for sample A, B and C is illustrated in Table 2.

4. Discussion

4.1. Elastic modulus of porous copper

In Fig. 5(a), we plot the elastic modulus obtained from the nanoindentation experiment and the modeling, as well as several correlations known from literature [49–55] that link the porosity with the elastic modulus.

For high porosity materials or foams with a porosity larger than 30 % [50], a simple scaling relation for the mechanical properties is derived by Gibson and Ashby [51]. It follows that the elastic modulus for a high porous material is, $E^* = E_s(1-P)^2$ where E^* and E_s are the elastic modulus of the porous solid and solid material, respectively, and P corresponds to the porosity. The scaling law according to [51] as illustrated in Fig. 5(a) does not describe the data well. The model illustrates a far too strong increase of the elastic modulus with decreasing porosity. According to Ashby et al. [52], the scaling law can be extended by using a pre-factor C, so that it can be written as $E^* = C\,E_s(1-P)^2$. The use of the

Table 1
Comparison between experimentally evaluated and FEM modeled material parameters.The mean value of the absolute porosity is labeled as P. The reduced elastic modulus obtained from the nanoindentation experiment and from the FEM modeling is labeled as E_{porous} and E_{FEM}, respectively. The specific electrical resistivity obtained from the 4-point probe measurement and FEM modeling is labeled as ρ_{porous} and ρ_{FEM}, respectively. All parameters are provided with the corresponding standard deviation (SD).

	Mean porosity P from FIB [%]	Reduced elastic modulus		Spec. resistivity	
		E_{porous} [GPa]	E_{FEM} [GPa]	ρ_{porous} [μΩ.cm]	ρ_{FEM} [μΩ.cm]
A	55.0 ± 4.1	14.8 ± 0.6	10.7 ± 3.6	14.4 ± 1.9	9.9 ± 2.7
B	31.2 ± 4.8	33.8 ± 2.2	39.4 ± 9.4	6.0 ± 0.9	3.9 ± 2.2
C	36.1 ± 1.7	29.8 ± 0.5	36.4 ± 4.5	4.4 ± 1.5	3.9 ± 1.7

modified scaling law in [52] with $C=0.66$, provides a better agreement with the presented data. Ashby et al. [52] stated that the factor C lies between 0.1 and 4 for open foams. The analytical model by Ramakrishnan and Arunachalam [53] is based on the proposed formula by Ashby et al. [52]. However, the pre-factor C is defined by $C = \frac{1}{1+(2-3\nu_s)P}$, with P and ν_s for the porosity and Poisson ratio, respectively.

A modified version of the above mentioned power equation is given by $E^* = E_s(1-jP)^i$ where j and i are material constants and E_s is the elastic modulus of the solid material [54]. The equation should meet the boundary conditions $E^* = E_s$ at $P = 0$ and $E^* = 0$ at $P \leq 1$. Using least square regression method, we obtain for j and i the values of 1 and 2.93, respectively. The material constant j can be defined as $j = 1/P_{crit}$,

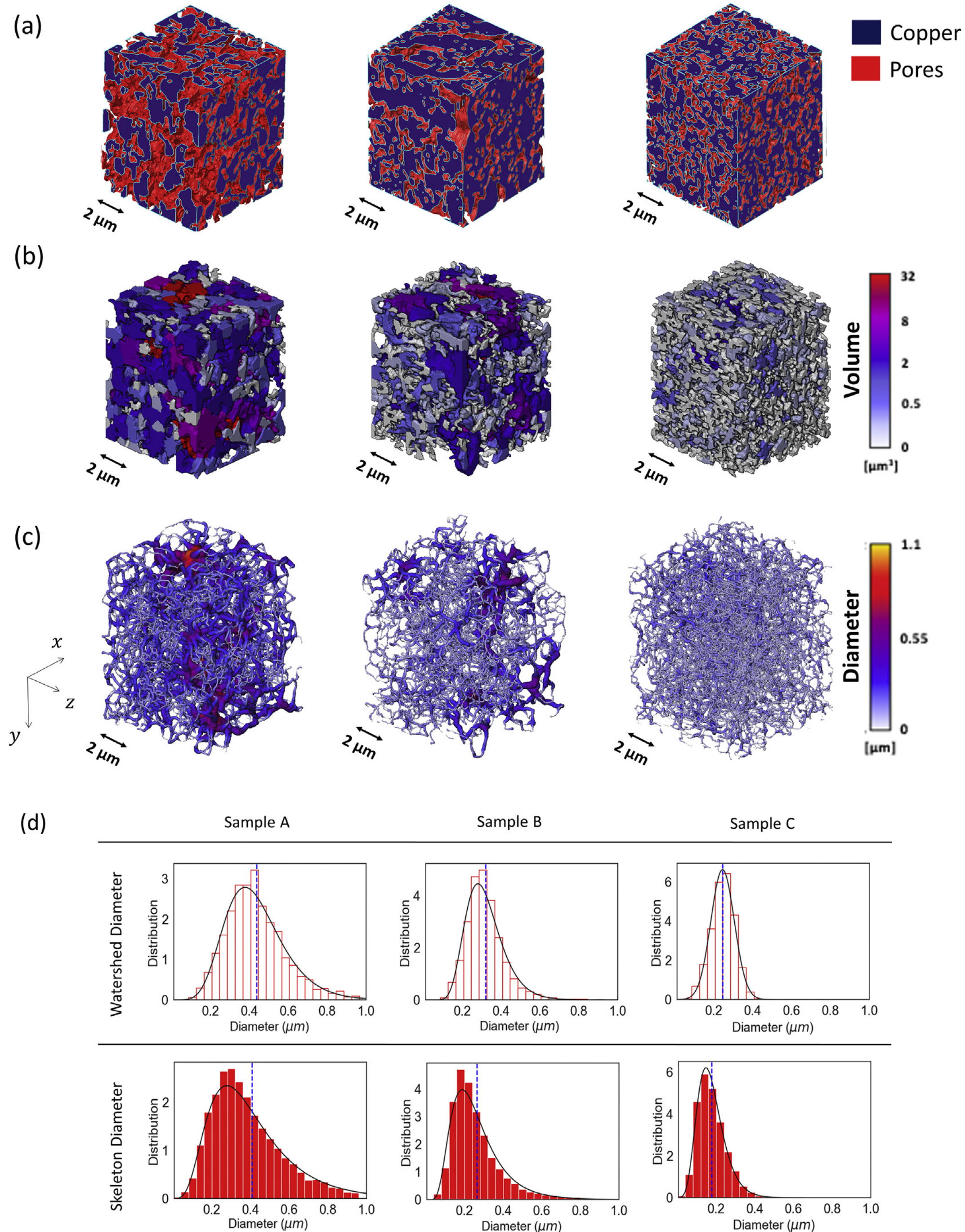

Fig. 3. Segmented 3D data for sample A, B and C (from left to right) using the hybrid image analysis method and pore size distribution. (a) Rendered binary 3D VOI with copper (dark blue) and pore phase (red). (b) Watershed algorithm applied for the three samples. The selected bin number is 2. The color refers to the volume of the individual pore segments i, with $i = 1,2,3,$ …. (c) Skeletonization of the three samples. The color code represents the local diameter of the pores. (d) The pore diameter size distribution obtained from the skeleton- and watershed-diameter analysis. The mean value of the diameter is highlighted as dashed line. (For interpretation of the references to color in this figure legend, the reader is referred to the web version of this article.)

Table 2
Quantified morphology parameters for sample A, B and C. Pore quantification showing the mean diameter $\overline{d}_{p,skel}$ obtained from the skeletonization algorithm as well as the mean hydraulic radius $\overline{r}_{p,watsh}$ and hydraulic diameter $\overline{d}_{p,watsh}$ applying the watershed algorithm. The evaluated mean diameter for the copper grains is presented by $\overline{d}_{grain}$. All parameters are provided with the corresponding standard deviation (SD).

	Skeletonization	Watershed segmentation				EBSD
	$\overline{d}_{p,skel}$ [nm]	$\overline{V}_p$ [µm³]	$\overline{A}_p$ [µm²]	$\overline{r}_{p,watsh}$ [nm]	$\overline{d}_{p,watsh}$ [nm]	$\overline{d}_{grain}$ [nm]
A	408 ± 227	1.63 ± 0.34	10.54 ± 1.45	109 ± 41	436 ± 157	244 ± 136
B	264 ± 133	0.60 ± 0.16	5.48 ± 0.87	79 ± 25	316 ± 99	382 ± 249
C	176 ± 720	0.18 ± 0.02	2.43 ± 0.16	61 ± 15	244 ± 60	279 ± 146

where P_{crit} is the critical porosity at which the elastic modulus becomes zero [55] and j is a packing geometry factor. It lies between the minimum value of 1 for a randomness packing with the maximum value $P_{crit} = 1$ and the maximum value of 3.84 for hexagonal closed packed structure. Since $j = 1$, it indicates that the elastic modulus of the material becomes zero only at 100 % porosity. The constant i or pore shape factor is dependent on the pore geometry and its orientation. According to Maitra and Phani [56], the exponent i is 2 for closed spherical pores and 4 for random orientated or irregular shaped pores. At high porosities and for an ordered packing the contact area is largely reduced, which leads to lower values of the elastic modulus. A high value of the elastic modulus at high porosity can be explained by a pore structure with a sort of randomness in packing.

Figure 5(a) shows all the fitting lines to the experimental and simulated results. We calculate the mean squared errors (MSE) of the fitting equations to the experimental and simulated data to assess the performed fits. The MSE of Gibson-Ashby [51], Ashby et al. [52], Ramakrishnan-Arunachalam [53], and Phani-Niyogi [54] are about 236.38 GPa^2, 11.33 GPa^2, 20.95 GPa^2, and 11.34 GPa^2, respectively. The fit according to [52] provides the lowest MSE using the fit parameter C=0.66. The collected and analyzed 3D image data shown in Fig. 3, respectively confirms that the sintered copper films display an open porous morphology. However, it might be argued that the defined range between 0.1 and 4 is quite large and unspecific. The Phani-Niyogi related fit [54] provides a similar MSE using the two variables $i = 2.93$ (random shaped pores) and $j = 1$ (randomness packing), representing

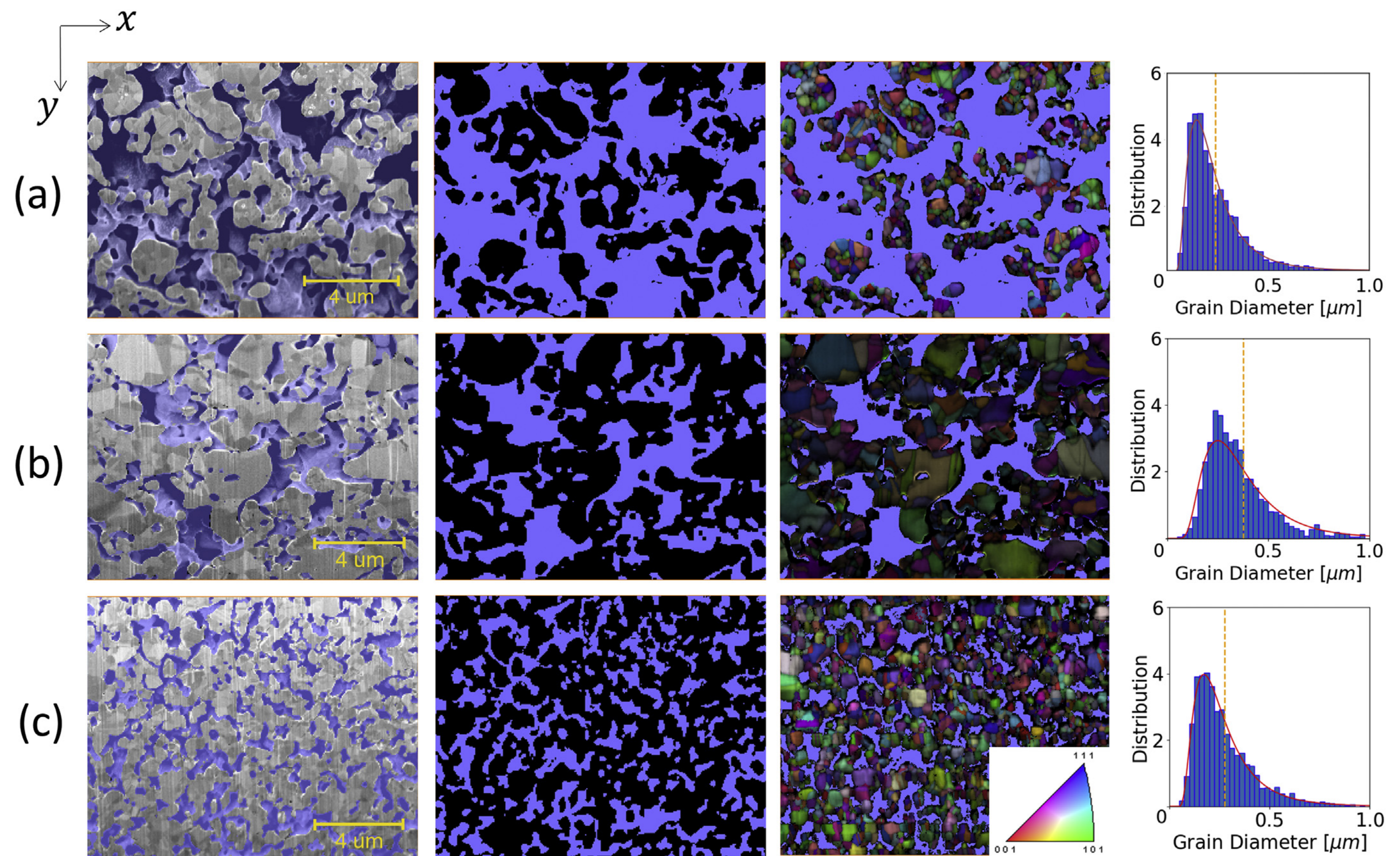

Fig. 4. Aanalyzed SEM/EBSD data. Left: SEM grey value data of a representative 2D slice and projected segmented pore phase (blue). Copper phase in original grey value. Middle: segmented copper (black) and pore phase (blue). Right: projected segmented pore phase on the SEM/EBSD (IPF-IQ) data. (a) Sample A, (b) sample B and (c) sample C with the corresponding grain size distribution (dashed lines show the corresponding means) obtained from the image processed SEM/EBSD data. Red line indicates the log-normal fit. The texture of all samples reveals an almost randomly orientated polycrystalline microstructure with no preferable crystal orientation as indicated by the color distribution. The shown scale bar applies to all images. (For interpretation of the references to color in this figure legend, the reader is referred to the web version of this article.)

the pore shape and packing geometry factor, respectively. The analyzed 3D image data exhibits channel-like structures with a randomness in packing as well as with non-closed random shaped pores (see Fig. 3). Both, the extracted values for the fitting parameters i and j suggest agreement with the pore morphology data. The third lowest MSE is given by the fit of Ramakrishnan and Arunachalam [53] where the fit parameter C is defined by the Poisson ratio of the solid material ν_s. That is, the trend of the elastic modulus of the porous solid versus porosity is mainly defined by the Poisson ratio of the solid material.

The modeling does not take the grain size of the copper into account. Therefore, one can conclude that due to the good correspondence between the results obtained from the experiment and modeling, the elastic modulus of the sintered copper films is mainly determined by the pore morphology. The obtained results in Fig. 5(a) and accordance of the fit [52,54] with Fig. 3 support the assumption that the elastic modulus is not necessarily influenced by the grain morphology of the sintered material [57].

4.2. Specific electrical resistivity of porous copper

In Fig. 5(b), we plot the specific electrical resistivity obtained from the 4-point probe experiment as well as from the modeling. We fit the specific electrical resistivity ρ with the porosity P according to the

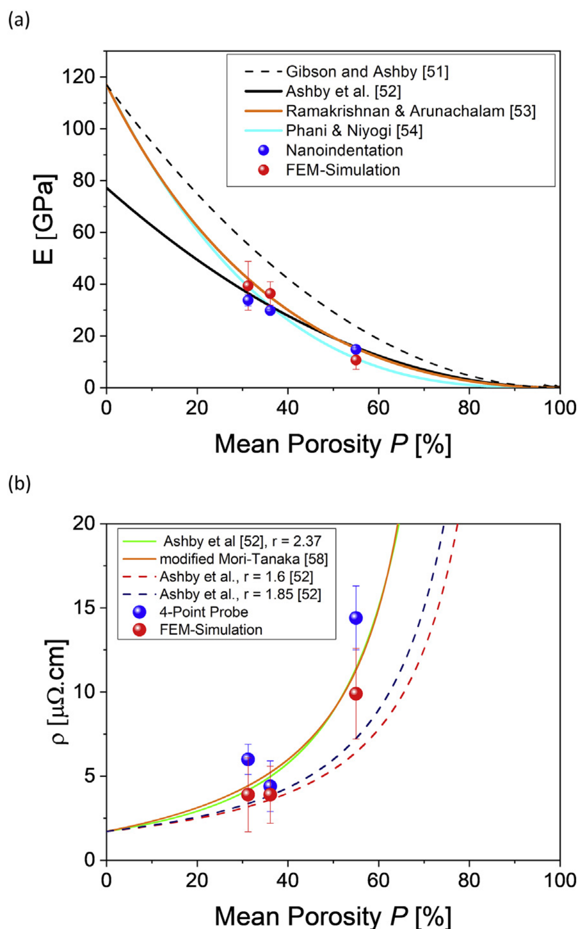

Fig. 5. (a) Elastic modulus as a function of the mean porosity P. Experimental nanoindentation data of sample A, B and C is compared with modeled data using RVE-FEM simulations. The RVE-FEM simulations use the segmented 3D morphology as input. Grain morphology of copper is not incorporated in the modeling. (b) Specific electrical resistivity as a function of the mean porosity P. Data for sample A, B and C is obtained from RVE-FEM simulations and 4-point probe measurements. Various models as indicated in the figure legend are used to fit the data for the elastic modulus and specific electrical resistivity.

simplified scaling law from Ashby et al. [52] with $\rho^* = \rho_{Cu}(1-P)^{-r}$, where ρ^* and ρ_{cu} are the specific resistivity of the porous and bulk copper respectively. The best fit to our data from least square method gives $r = 2.37$. The exponent r according to [52] is defined between 1.60 and 1.85 for open and closed cell foams, respectively.

The fit for $r = 1.60$ and 1.85 is shown in Fig. 5(b) with a red and blue dashed line, respectively.

In addition, we use in Fig. 5(b) the relationship based on the modified Mori-Tanaka relationship [58] with $\rho = \rho_0 \frac{1+kP}{1-P/P_{crit}}$, where ρ and ρ_0 correspond to the electrical resistivity of the porous and bulk materials, respectively, P is the porosity, P_{crit} is the critical porosity, and k is the characteristic constant. The least square fit gives for P_{crit} and k, the values 0.79 and 1.78, respectively. According to the model [58] the characteristic constant $k = 0.5$ for spherical pores.

The MSE for [52,58] provides 2.69 and 2.79 $(\mu\Omega.\text{cm})^2$ respectively. The evaluated r value of 2.37 for the model described in [52] is not defined. A distinction according to [52] between open and closed pores is not possible. The modified Mori-Tanaka [58] provides for P_{crit} and k, the values 0.79 and 1.78, that is $k > 0.5$. This finding is in correspondence with the analyzed morphology, illustrated in Fig. 3, where a non-spherical pore geometry is depicted. Further, the evaluated value of P_{crit} with 0.79 is similar to porous titanium with $P_{crit} = 0.81$ reported in [58].

However, the fit does not clarify the discrepancy shown in the simulation and the experimental data as shown in Fig. 5(b) and Table 1.

In order to link the electrical resistivity with the 3D morphology, we extract the spatial geometric tortuosity for the copper along the y- direction. The y- direction displays the most relevant direction for the current flow, which corresponds to the direction perpendicular to the [100] Si-substrate. Further data along the x- and z- direction are presented in Supplementary 4. In Fig. 6(a), we quantify the spatial geometric tortuosity to visualize the change of the 3D copper network-connectivity for sample A, B and C. Dark blue in the color code indicates low tortuosity. Meaning the ratio between the path through the pore network and the direct distance is small, i.e., the value is close to 1. A change of the color from blue towards yellow means that the path is getting more tortuous and the electrical conductivity decreases. Fig. 6(b) shows the spatial geometric tortuosity along the y- direction in the x-z- plane for a representative slice at about $y = 4.37$ µm. Here, the significant variation of the tortuosity can be observed locally within the copper regions. Clearly, we can see in Fig. 6 for the 3D- as well as the 2D-representation that the path through the copper is more tortuous for sample A than for sample B and C.

According to the simulations, sample B and C provide similar resistivity values although the porosity of sample B is about 5 % lower than for sample C, see Table 1.

We argue that the similar simulated specific resistivity of 3.9 ± 2.2 µΩ.cm and 3.9 ± 1.7 µΩ.cm for sample B and C, respectively in the modeling might be explained by the similar geometric tortuosity behavior of the copper observed for the two samples. Nevertheless, as shown in Table 1 the observed modeling result is in contradiction with the experimental results.

The 4-point probe measurements provide 6.0 ± 0.9 µΩ.cm and 4.4 ± 1.5 µΩ.cm for sample B and C, respectively (Table 1). The contradiction between the model and the experiment might be explained by taking the grain morphology into account. The observed distribution of sample B (Fig. 4(b)) after the sinter process admits small as well as large grains to grow. Although the grain morphology for sample A and C is similar, there exists a major difference with respect to the pore morphology. Sample C shows, in comparison to sample A, a smaller porosity (Table 1), a lower geometric tortuosity of the copper along y- direction (Fig. 6) and a different pore diameter distribution with a smaller mean pore diameter as well as a smaller standard deviation (Fig. 3(d) and Table 2). Those observed differences in the pore morphology suggest to trigger the different electrical behavior observed for sample A and

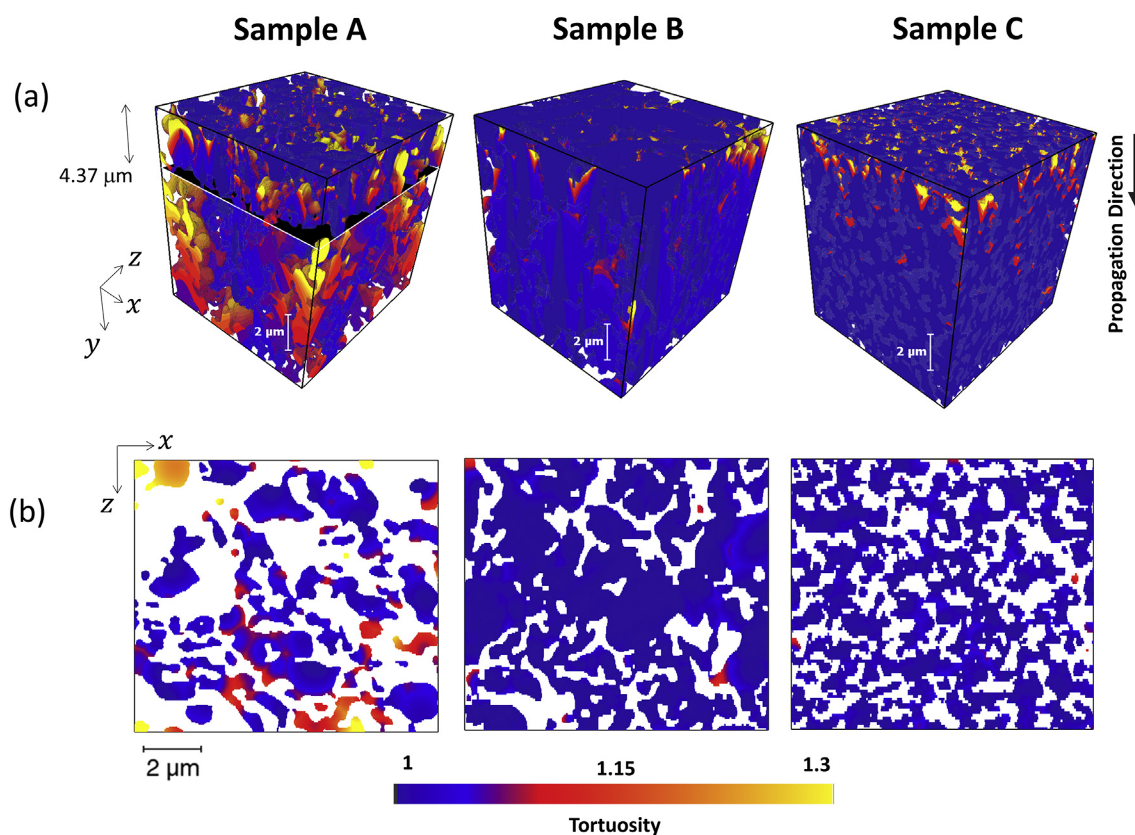

Fig. 6. Spatial geometric tortuosity. (a) Spatial geometric tortuosity of the copper in 3D for sample A, B and C (from left to right). The propagation direction is in *y*- direction for sample A, B and C. Dark blue indicates a tortuosity of 1, i.e., only small deviations from the direct distance. Yellow indicates regions that are hard to reach for electrons coming from the surface and traveling in *y*- direction through the sample. We plot the tortuosity between 1 and 1.3. In sample A, we indicate the position of the representative slice used in the 2D representation, at $y = 4.37$ μm. (b) Spatial geometric tortuosity distribution in the *z*-*x*- plane (2D) at $y = 4.37$ μm for the copper region. Color code as for the 3D representation in (a). Sample A indicates for the same area of interest a higher tortuosity within the copper than for sample B and C. B and C show similar color coding, that is similar geometrical tortuosity. Pore space is shown in white. (For interpretation of the references to color in this figure legend, the reader is referred to the web version of this article.)

C, as indicated in Table 1. Therefore, sample A shows a rather high specific resistivity with 14.4 ± 1.9 μΩ.cm in comparison to sample C as well as to sample B with 4.4 ± 1.5 μΩ.cm and 6.0 ± 0.9 μΩ.cm, respectively. We conclude that the low specific electrical resistivity of about 4.4 μΩ cm ± 1.5 μΩ.cm from sample C with a porosity of 36.1 ± 1.7 % can be explained by taking the pore and copper morphology into account. The observed electrical and elastic properties are mainly determined by the homogeneous copper grain- size distribution (Fig. 4) as well as the low spatial geometric tortuosity of the copper fraction along the *y*- direction (Fig. 6) and homogeneous pore size distribution (Fig. 3(d)).

5. Conclusion

In this paper we present a multi-method characterization approach to understand the impact of the morphology on the elastic as well as electrical behavior. Nano-SEM/FIB tomography and SEM/EBSD are applied to probe the morphology of three representative copper films. Nanoindentation and 4-point probe are used to extract the elastic modulus and specific electrical resistivity. The evaluated material parameters are compared with modeling results using the analyzed image data as an input.

For the crucial image analysis, we develop a validated objective image analysis workflow to provide accurate information regarding the pore and copper morphology without the need to use infiltration for contrast enhancement [26,27]. We extract pore morphology parameters like the porosity, and mean pore diameters, pore size distributions, as well as copper morphology parameters including the grain size distribution of the copper, and spatial geometric tortuosity of the copper. We obtain a quantified insight about the effect of the heterogeneous morphologies on the elastic modulus and specific electrical resistivity, thereby delivering important information about the necessary homogeneous copper grain- and nano-scale pore-design.

Notably, the elastic modulus of the investigated sintered copper films mainly is determined by the pore morphology. The scaling model provided by Ashby et al. [52], as well as the model of Phani-Niyogi [54] provide the best fit results for the sintered copper films with respect to the effect of the porosity on the elastic modulus. To understand the electrical properties of the sintered copper films, the grain morphology of the copper, the tortuosity of the copper as well as the pore morphology needs to be considered.

The approach facilitates a strategy to design the relevant material parameters by tuning the morphology. We show that this strategy enables us to systematically design a porous copper film for die-attach applications, which exhibits a low elastic modulus of about 29.8 ± 0.5 GPa with a low specific resistivity of about 4.4 ± 1.5 μΩ.cm, at 36.1 ± 1.7 % porosity.

Data availability

The raw/processed data required to reproduce these findings cannot be shared at this time as the data also forms part of an ongoing study.

Author statement

A. Wijaya: Methodology, Software, Investigation, Visualization, Formal analysis, Validation, Writing – Original Draft. B. Eichinger: Resources, Investigation. F. F. Chamasemani: Methodology, Investigation, Visualization. B. Sartory: Investigation. R. Hammer: Software, Validation, Investigation, Writing – Review & Editing. V. Maier-Kiener: Methodology, Investigation, Validation, Writing – Review and Editing. D. Kiener: Investigation, Writing – Review & Editing. M. Mischitz: Supervision, Resources, Writing – Review and Editing. R. Brunner: Writing – Original Draft, Writing – Review and Editing, Investigation, Methodology, Conceptualization, Supervision, Writing, Visualization, Reviewing, Funding acquisition.

Declaration of Competing Interest

The authors declare that they have no known competing financial interests or personal relationships that could have appeared to influence the work reported in this paper.

Acknowledgement

We acknowledge the contribution by the master student Juliane Kampichler taking part at the nanoindentation experiments. This work was supported by Die Österreichische Forschungsförderungsgesellschaft (FFG) [Produktion der Zukunft No. 853467 “ProQualiKu”] and partly by the Austrian Federal Ministries for Climate Action, Environment, Energy, Mobility, Innovation and Technology (BMK) and for Digital and Economic Affairs (BMDW), represented by the Austrian research funding association (FFG), and the federal states of Styria, Upper Austria and Tyrol within the framework of the COMET Funding Program (No. 859480).

Appendix A. Supplementary data

Supplementary data to this article can be found online at https://doi.org/10.1016/j.matdes.2020.109188.

References

[1] J. Biener, M.M. Biener, R.J. Madix, C.M. Friend, Nanoporous gold: understanding the origin of the reactivity of a 21st century catalyst made by pre-Columbian technology, ACS Catal. 5 (11) (Nov. 2015) 6263–6270, https://doi.org/10.1021/acscatal.5b01586.

[2] M.P. Hablitzel, E.T. Lilleodden, On measuring the independent mechanical response of the polymer phase from nanoporous gold polymer composites, Scr. Mater. 170 (Sep. 2019) 67–70, https://doi.org/10.1016/j.scriptamat.2019.04.026.

[3] V. Håkonsen, G. Singh, J. He, Z. Zhang, Focused ion beam milling of self-assembled magnetic superstructures: an approach to fabricate nanoporous materials with tunable porosity, Mater. Horizons 5 (6) (Nov. 2018) 1211–1218, https://doi.org/10.1039/c8mh01112e.

[4] I.V. Okulov, et al., Nanoporous magnesium, Nano Res. 11 (12) (Dec. 2018) 6428–6435, https://doi.org/10.1007/s12274-018-2167-9.

[5] A. Baux, et al., Digitization and image-based structure-properties relationship evaluation of a porous gold micro-electrode, Mater. Des. 193 (Aug. 2020) 108812, https://doi.org/10.1016/j.matdes.2020.108812.

[6] L. Cao, Q. Fu, Y. Si, B. Ding, J. Yu, Porous materials for sound absorption, Composites Communications, vol. 10, Elsevier Ltd Dec. 01, 2018, pp. 25–35, https://doi.org/10.1016/j.coco.2018.05.001.

[7] D. Ishikawa, et al., Copper Die-Bonding Sinter Paste: Sintering and Bonding Properties, Nov. 2018https://doi.org/10.1109/ESTC.2018.8546455.

[8] Y. Peng, W. Zhu, S. Shen, L. Feng, Y. Deng, Bottom-up sandwich-porous copper films: facile construction, growth mechanism, and super-elastic property, Mater. Des. 135 (Dec. 2017) 151–158, https://doi.org/10.1016/j.matdes.2017.09.022.

[9] K. Wang, C. Stenner, J. Weissmüller, A nanoporous gold-polypyrrole hybrid nanomaterial for actuation, Sensors Actuators B Chem. 248 (Sep. 2017) 622–629, https://doi.org/10.1016/j.snb.2017.04.025.

[10] Q. Zhang, et al., Bamboo-inspired lightweight tape suture with hollow and porous structure for tendon repair, Mater. Des. 193 (Aug. 2020) 108843, https://doi.org/10.1016/j.matdes.2020.108843.

[11] M.H. Kang, et al., Biomimetic porous mg with tunable mechanical properties and biodegradation rates for bone regeneration, Acta Biomater. 84 (Jan. 2019) 453–467, https://doi.org/10.1016/j.actbio.2018.11.045.

[12] K. Mohan, N. Shahane, R. Liu, V. Smet, A. Antoniou, A review of nanoporous metals in interconnects, JOM 70 (10) (Oct. 01, 2018) 2192–2204, https://doi.org/10.1007/s11837-018-3081-z Minerals, Metals and Materials Society.

[13] L. Lorenz, Power semiconductor devices and smart power IC's - The enabling technology for future high efficient power conversion systems, 2009 IEEE 6th International Power Electronics and Motion Control Conference, 09, IPEMC 2009, pp. 193–201, https://doi.org/10.1109/IPEMC.2009.5289338.

[14] X. Guo, Q. Xun, Z. Li, S. Du, Silicon carbide converters and MEMS devices for high-temperature power electronics: A critical review, Micromachines 10 (6) (2019) https://doi.org/10.3390/mi10060406 MDPI AG, Jun. 01.

[15] P. Herfurth, et al., GaN-on-insulator technology for high-temperature electronics beyond 400 °c, Semicond. Sci. Technol. 28 (7) (Jul. 2013) 074026, https://doi.org/10.1088/0268-1242/28/7/074026.

[16] S. Brand, et al., Non-destructive assessment of the porosity in silver (Ag) sinter joints using acoustic waves, Proceedings - Electronic Components and Technology Conference, 2018-May, Aug. 2018, pp. 1863–1870, https://doi.org/10.1109/ECTC.2018.00279.

[17] C. Buttay, B. Allard, R. Riva, Silver sintering for power electronics integration, ICEP-IAAC 2015–2015 International Conference on Electronic Packaging and iMAPS All Asia Conference May 2015, pp. 554–558, https://doi.org/10.1109/ICEP-IAAC.2015.7111076.

[18] W. Schmitt, L.M. Chew, Silver sinter paste for SiC bonding with improved mechanical properties, Proceedings - Electronic Components and Technology Conference Aug. 2017, pp. 1560–1565, https://doi.org/10.1109/ECTC.2017.155.

[19] R. Treml, et al., High resolution determination of local residual stress gradients in single- and multilayer thin film systems, Acta Mater. 103 (Jan. 2016) 616–623, https://doi.org/10.1016/j.actamat.2015.10.044.

[20] E. Grünwald, et al., Advanced 3D failure characterization in multi-layered PCBs, NDT E Int. 84 (Dec. 2016) 99–107, https://doi.org/10.1016/j.ndteint.2016.08.003.

[21] S.S. Tonapi, R.A. Fillion, F.J. Schattenmann, H.S. Cole, J.D. Evans, B.G. Sammakia, An overview of thermal management for next generation microelectronic devices, ASMC (Advanced Semiconductor Manufacturing Conference) Proceedings, 2003-January, 2003, pp. 250–254, https://doi.org/10.1109/ASMC.2003.1194502.

[22] M. Knoerr, S. Kraft, A. Schletz, Reliability assessment of sintered nano-silver die attachment for power semiconductors, 2010 12th Electronics Packaging Technology Conference, EPTC 2010 2010, pp. 56–61, https://doi.org/10.1109/EPTC.2010.5702605.

[23] V.R. Manikam, K.Y. Cheong, Die attach materials for high temperature applications: a review, IEEE Trans. Compon. Packag. Manuf. Technol. 1 (4) (2011) 457–478, https://doi.org/10.1109/TCPMT.2010.2100432.

[24] A. Etiemble, A. Tranchot, T. Douillard, H. Idrissi, E. Maire, L. Roué, Evolution of the 3D microstructure of a Si-based electrode for Li-ion batteries investigated by FIB/SEM tomography, J. Electrochem. Soc. 163 (8) (2016) A1550–A1559, https://doi.org/10.1149/2.0421608jes.

[25] J.A. Taillon, C. Pellegrinelli, Y.L. Huang, E.D. Wachsman, L.G. Salamanca-Riba, Improving microstructural quantification in FIB/SEM nanotomography, Ultramicroscopy 184 (Jan. 2018) 24–38, https://doi.org/10.1016/j.ultramic.2017.07.017.

[26] Z. Chen, X. Wang, F. Giuliani, A. Atkinson, Microstructural characteristics and elastic modulus of porous solids, Acta Mater. 89 (May 2015) 268–277, https://doi.org/10.1016/j.actamat.2015.02.014.

[27] M. Ziehmer, K. Hu, K. Wang, E.T. Lilleodden, A principle curvatures analysis of the isothermal evolution of nanoporous gold: quantifying the characteristic length-scales, Acta Mater. 120 (Nov. 2016) 24–31, https://doi.org/10.1016/j.actamat.2016.08.028.

[28] K. Mohan, N. Shahane, P.M. Raj, A. Antoniou, V. Smet, R. Tummala, Low-temperature, organics-free sintering of nanoporous copper for reliable, high-temperature and high-power die-attach interconnections, Conference Proceedings - IEEE Applied Power Electronics Conference and Exposition - APEC May 2017, pp. 3083–3090, https://doi.org/10.1109/APEC.2017.7931137.

[29] T. Maitland, S. Sitzman, Electron Backscatter Diffraction (EBSD) Technique and Materials Characterization Examples, 2015.

[30] W.C. Oliver, G.M. Pharr, An improved technique for determining hardness and elastic modulus using load and displacement sensing indentation experiments, J. Mater. Res. 7 (6) (Jun. 1992) 1564–1583, https://doi.org/10.1557/jmr.1992.1564.

[31] I. Miccoli, F. Edler, H. Pfnür, C. Tegenkamp, The 100th anniversary of the four-point probe technique: The role of probe geometries in isotropic and anisotropic systems, J. Phys. Condens. Matter 27 (22) (Jun. 10, 2015) 223201, https://doi.org/10.1088/0953-8984/27/22/223201 Institute of Physics Publishing.

[32] A. Vedaldi, S. Soatto, Quick Shift and Kernel Methods for Mode Seeking, Springer, Berlin, Heidelberg, 2008 705–718.

[33] P.F. Felzenszwalb, D.P. Huttenlocher, Efficient graph-based image segmentation, Int. J. Comput. Vis. 59 (2) (Sep. 2004) 167–181, https://doi.org/10.1023/B:VISI.0000022288.19776.77.

[34] R. Achanta, A. Shaji, K. Smith, A. Lucchi, P. Fua, S. Süsstrunk, SLIC superpixels compared to state-of-the-art superpixel methods, IEEE Trans. Pattern Anal. Mach. Intell. 34 (11) (2012) 2274–2281, https://doi.org/10.1109/TPAMI.2012.120.

[35] N. Otsu, Threshold selection method from GRAY-level histograms, IEEE Trans Syst Man Cybern SMC-9 (1) (1979) 62–66, https://doi.org/10.1109/tsmc.1979.4310076.

[36] M. Sezgin, S. Bulent, Survey over image thresholding techniques and quantitative performance evaluation, J. Electron. Imaging 13 (1) (Jan. 2004) 146, https://doi.org/10.1117/1.1631315.

[37] P.K. Saha, G. Borgefors, G. Sanniti di Baja, A survey on skeletonization algorithms and their applications, Pattern Recogn. Lett. 76 (Jun. 2016) 3–12, https://doi.org/10.1016/j.patrec.2015.04.006.

[38] P. Iassonov, T. Gebrenegus, M. Tuller, Segmentation of X-ray computed tomography images of porous materials: A crucial step for characterization and quantitative

analysis of pore structures, Water Resour. Res. 45 (9) (Sep. 2009)https://doi.org/10.1029/2009WR008087.
[39] E. Dougherty, S. Beucher, F. Meyer, The morphological approach to segmentation: the watershed transformation, Mathematical Morphology in Image Processing, CRC Press 2019, pp. 433–481.
[40] G. Tomás, D. Martins, D. Cooper, G. Bonfait, Low-temperature thermal conductivity of highly porous copper, IOP Conference Series: Materials Science and Engineering, vol. 101, , Dec. 2015https://doi.org/10.1088/1757-899X/101/1/012004 , no. 1, p. 012004.
[41] M. Li, D. Wilkinson, K. Patchigolla, Comparison of particle size distributions measured using different techniques, Part. Sci. Technol. 23 (3) (Jul. 2005) 265–284, https://doi.org/10.1080/02726350590955912.
[42] T. Kanit, S. Forest, I. Galliet, V. Mounoury, D. Jeulin, Determination of the size of the representative volume element for random composites: statistical and numerical approach, Int. J. Solids Struct. 40 (13–14) (Jun. 2003) 3647–3679, https://doi.org/10.1016/S0020-7683(03)00143-4.
[43] S. Bigl, T. Schöberl, S. Wurster, M.J. Cordill, D. Kiener, Correlative microstructure and topography informed nanoindentation of copper films, Surf. Coat. Technol. 308 (Dec. 2016) 404–413, https://doi.org/10.1016/j.surfcoat.2016.07.104.
[44] P. Vannucci, Anisotropic Elasticity, vol. 85, Springer Singapore, Singapore, 2018.
[45] M. Schmitt, M. Halisch, C. Müller, C.P. Fernandes, Classification and quantification of pore shapes in sandstone reservoir rocks with 3-D X-ray micro-computed tomography, Solid Earth Discuss. 7 (4) (Dec. 2015) 3441–3479, https://doi.org/10.5194/sed-7-3441-2015.
[46] C. Fouard, G. Malandain, S. Prohaska, M. Westerhoff, Blockwise processing applied to brain microvascular network study, IEEE Trans. Med. Imaging 25 (10) (Oct. 2006) 1319–1328, https://doi.org/10.1109/TMI.2006.880670.
[47] K.K. Aligizaki, Pore Structure of Cement-Based Materials: Testing, Interpretation and, CRC Press, 2004.
[48] F.M. White, Viscous Flow in Ducts, Fluid Mechanics 4th Edition 1998, p. 358.
[49] W. Pabst, E. Gregorová, G. Tichá, Elasticity of porous ceramics - a critical study of modulus-porosity relations, J. Eur. Ceram. Soc. 26 (7) (Jan. 2006) 1085–1097, https://doi.org/10.1016/j.jeurceramsoc.2005.01.041.
[50] G. Lu, G.Q. Lu, Z.M. Xiao, Mechanical properties of porous materials, J. Porous. Mater. 6 (4) (1999) 359–368, https://doi.org/10.1023/A:1009669730778.
[51] L.J. Gibson, M.F. Ashby, Cellular Solids: Structure and Properties, Second Edition, Cambridge University Press, 2014.
[52] M. Ashby, T. Evans, N. Fleck, J.W. Hutchinson, H.N.G. Wadley, L.J. Gibson, Metal Foams: A Design Guide - 1st Edition, Butterworth-Heinemann, 2000.
[53] N. Ramakrishnan, V.S. Arunachalam, Effective elastic moduli of porous solids, J. Mater. Sci. 25 (9) (Sep. 1990) 3930–3937, https://doi.org/10.1007/BF00582462.
[54] K.K. Phani, S.K. Niyogi, Young's modulus of porous brittle solids, J. Mater. Sci. 22 (1) (Jan. 1987) 257–263, https://doi.org/10.1007/BF01160581.
[55] J.A. Choren, S.M. Heinrich, M.B. Silver-Thorn, Young's modulus and volume porosity relationships for additive manufacturing applications, J. Mater. Sci. 48 (15) (Aug. 02, 2013) 5103–5112, https://doi.org/10.1007/s10853-013-7237-5 Springer.
[56] A.K. Maitra, K.K. Phani, Ultrasonic evaluation of elastic parameters of sintered powder compacts, J. Mater. Sci. 29 (17) (Jan. 1994) 4415–4419, https://doi.org/10.1007/BF00376263.
[57] J. Carr, X. Milhet, P. Gadaud, S.A.E. Boyer, G.E. Thompson, P. Lee, Quantitative characterization of porosity and determination of elastic modulus for sintered micro-silver joints, J. Mater. Process. Technol. 225 (Jun. 2015) 19–23, https://doi.org/10.1016/j.jmatprotec.2015.03.037.
[58] K. Zhu, C.F. Li, Z.G. Zhu, Measurement of electrical conductivity of porous titanium and Ti6Al4V prepared by the powder metallurgy method, Chin. Phys. Lett. 24 (1) (Jan. 2007) 187–190, https://doi.org/10.1088/0256-307X/24/1/051.